Evaluation of Diffusion Techniques for Improved Vessel Visualization and Quantification in Three-Dimensional Rotational Angiography

Erik Meijering[1], Wiro Niessen[1], Joachim Weickert[2], and Max Viergever[1]

[1] Image Sciences Institute, University Medical Center Utrecht, Heidelberglaan 100, NL-3584 CX Utrecht, the Netherlands.
{erik,wiro,max}@isi.uu.nl
http://www.isi.uu.nl/

[2] Computer Vision, Graphics and Pattern Recognition Group, Department of Mathematics and Computer Science, University of Mannheim, D-68131 Mannheim, Germany.
Joachim.Weickert@uni-mannheim.de
http://www.cvgpr.uni-mannheim.de/weickert/

Abstract. Three-dimensional rotational angiography (3DRA) is a promising imaging technique which yields high-resolution isotropic 3D images of vascular structures. Raw 3DRA images, however, usually suffer from a high noise level and the presence of other artifacts. For accurate visualization and quantification of vascular anomalies, noise reduction is therefore highly desirable. In this paper we analyze the effects of several linear and nonlinear filtering techniques for that purpose. From the results of *in vitro* experiments we conclude that edge-enhancing anisotropic diffusion is very suitable for mentioned tasks. However, in view of the computational requirements of this technique, the regularized isotropic nonlinear diffusion scheme may be considered a useful alternative.

1 Introduction

Three-dimensional rotational angiography (3DRA) is a relatively new technique for imaging blood vessels in the human body [1,2,3,4,5]. Using a standard C-arm imaging system, this technique yields high-resolution isotropic 3D datasets reconstructed from 2D X-ray angiography images acquired during a 180-degree rotation of the X-ray source-detector combination following a single injection of contrast material. The vascular structures of interest can afterwards be studied from any desired angle by the use of 3D visualization techniques. The absence of overprojections and the high resolution of the resulting datasets make the technique also potentially interesting for quantitative studies.

However, visualization of raw 3DRA images is usually unacceptable, due to the high noise level and the presence of reconstruction artifacts and unwanted structures resulting from inhomogeneous surrounding tissue. In order to improve

W. Niessen and M. Viergever (Eds.): MICCAI 2001, LNCS 2208, pp. 177–185, 2001.

the quality of volume and surface renderings, some form of noise reduction must be applied to the raw data prior to visualization. Although application of noise reduction techniques may result in qualitatively better renderings, the effects of such techniques on the subsequent quantification of vessels and vascular anomalies based on those renderings have not yet been reported in the literature. Analysis of these effects is important, as particular techniques may increase the user-dependency of volume and surface renderings—which are generally based on one or more user-defined thresholds—and thus the reliability of quantitative measurements obtained from those renderings. In this paper we evaluate several linear and nonlinear diffusion filtering techniques for noise reduction by analyzing their effects on the quality of visualization and the accuracy of quantification of vascular anomalies in 3DRA images.

2 Diffusion Techniques

The noise reduction techniques considered in this study are uniform filtering, Gaussian filtering or linear diffusion, regularized isotropic nonlinear diffusion, and edge-enhancing anisotropic diffusion, which are briefly described next.

Uniform Filtering. The simplest and computationally cheapest approach to reduce noise in images is to average the grey-values of voxels in a cubic neighborhood around each voxel by means of separable uniform filtering (UF):

$$I(\mathbf{x}) = (I_0 * U_m)(\mathbf{x}), \qquad \mathbf{x} = (x, y, z) \in X, \tag{1}$$

where I_0 denotes the original 3D image, $X \subset \mathbb{R}^3$ is the image domain, and $U_m(\mathbf{x}) = u_m(x)u_m(y)u_m(z)$ denotes the 3D normalized uniform filter given by $u_m(\xi) = m^{-1}$ if $|\xi| \leq \frac{1}{2}m$, $m \in \mathbb{N}$ odd, and $u_m(\xi) = 0$ otherwise.

Gaussian Filtering. Another frequently used approach to image smoothing is Gaussian filtering (GF), also implemented by separable convolution:

$$I(\mathbf{x}) = (I_0 * G_\sigma)(\mathbf{x}), \qquad \mathbf{x} = (x, y, z) \in X, \tag{2}$$

with $G_\sigma(\mathbf{x}) = g_\sigma(x)g_\sigma(y)g_\sigma(z)$, and g_σ denoting the Gaussian with standard deviation σ. The process (2) constitutes the solution to the linear diffusion equation $\partial_t I(\mathbf{x};t) = \nabla \cdot \nabla I(\mathbf{x};t)$, with $\sigma = \sqrt{2t}$ and initial condition $I(\mathbf{x};0) = I_0(\mathbf{x})$.

Regularized Isotropic Nonlinear Diffusion. The first nonlinear technique included in this study is the regularized version of the Perona-Malik scheme [6]. This scheme (RPM) is obtained from the linear diffusion equation by including a gradient-dependent diffusivity:

$$\partial_t I(\mathbf{x};t) = \nabla \cdot \Big(D\big(\|\nabla I_\tau(\mathbf{x};t)\|^2\big) \nabla I(\mathbf{x};t) \Big), \tag{3}$$

where the gradient is computed at scale $\sigma_n = \sqrt{2\tau}$, $\tau > 0$. In our study, we used [7] $D\big(\xi^2\big) = 1 - \exp\big(-3.31488/(\xi/\zeta)^8\big)$, where $\zeta > 0$ corresponds to the minimum contrast needed for structures in order to be preserved.

Edge-Enhancing Anisotropic Diffusion. The second nonlinear diffusion technique (EED) does not only take into account the contrast of an edge, but also its orientation. This is achieved by replacing the scalar-valued diffusivity in (3) by a diffusion tensor [7]:

$$\partial_t I(\mathbf{x};t) = \nabla \cdot \Big(\mathbf{D}\big(\nabla I_\tau(\mathbf{x};t)\big) \nabla I(\mathbf{x};t) \Big), \tag{4}$$

where $\mathbf{D}$ is constructed from the system of orthonormal eigenvectors $\mathbf{v}_1 \| \nabla I(\mathbf{x};\tau)$, $\mathbf{v}_2 \perp \nabla I(\mathbf{x};\tau)$, $\mathbf{v}_3 \perp \nabla I(\mathbf{x};\tau)$ and $\perp \mathbf{v}_2$, and corresponding eigenvectors $\lambda_1 = D\big(\|\nabla I(\mathbf{x};\tau)\|^2\big)$ and $\lambda_2 = \lambda_3 = D(0) = 1$, with D as in RPM. With this choice of $\mathbf{D}$, smoothing along edges is preferred over smoothing across them.

3 Vascular Anomalies

Currently, 3DRA is used primarily for visualization and subsequent quantification of carotid stenosis and intracranial aneurysms [3,4,5]. We briefly discuss the measures used for quantification of these anomalies.

Carotid Stenosis. For the quantification of the degree of stenosis of the internal carotid artery (ICA) we used the North American Symptomatic Carotid Endarterectomy Trial (NASCET) measure and the common carotid measure (CC) [8], respectively defined as $D_{\text{NASCET}} = (1 - d_{\text{S}}/d_{\text{ICA}})$ and $D_{\text{CC}} = (1 - d_{\text{S}}/d_{\text{CCA}})$, with d_{S}, d_{ICA}, and d_{CCA} as in Fig. 1. Both measures involve measuring the luminal diameter at the point of maximum stenosis (d_{S}). The NASCET measure furthermore involves the diameter (d_{ICA}) of a visible portion of disease-free ICA distal to the stenosis, whereas the CC measure uses the diameter (d_{CCA}) of the visible disease-free distal common carotid artery (CCA).

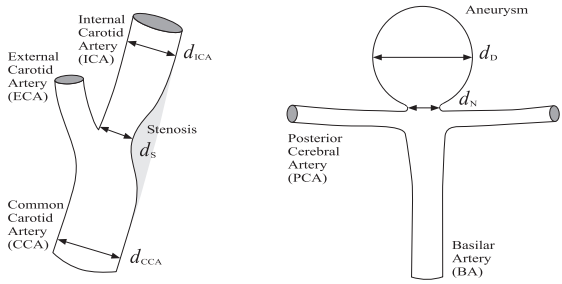

Fig. 1. Diameters involved in the different measures for quantification of internal carotid stenosis (**left**) and intracranial saccular aneurysms (**right**).

Intracranial Aneurysms. For quantification of intracranial aneurysms, several measures were considered. The first is the dome diameter (d_{D}, see Fig. 1), which has been shown to relate significantly to risk of rupture [9]. The second measure considered in this study is the diameter of the aneurysmal neck (d_{N}), which is important in selecting an appropriate clip in the case of surgical intervention or for predicting successful obliteration of the aneurysmal lumen in the case of endovascular treatment [10]. The ratio between diameters d_{N} and d_{D} of the aneurysm has also been suggested as a guideline in deciding between surgical or endovascular treatment [11].

4 Experiments and Results

The experiments were carried out on phantoms for which ground truth was available. In this section we describe the phantoms and image acquisition, the method of evaluation, and the results.

Phantoms and Image Acquisition. Images were obtained of a carotid anthropomorphic vascular phantom (CAVP) with an asymmetrical stenosis in the ICA, and an intracranial anthropomorphic vascular phantom (IAVP) with a berry aneurysm at the tip of the basilar artery (BA). The phantoms (R. G. Shelley Ltd., North York, Ontario) represent average dimensions of the corresponding vascular structures in the human body: $d_{\mathrm{S}} = 1.68$mm, $d_{\mathrm{ICA}} = 5.6$mm, $d_{\mathrm{CCA}} = 8.0$mm, $d_{\mathrm{N}} = 2.6$mm, and $d_{\mathrm{D}} = 12.9$mm. Each of the phantoms was filled with contrast material (50% diluted Ultravist-300, Schering, Weesp) and an Integris V3000 C-arm imaging system (Philips Medical Systems, Best) was used to acquire 100 X-ray angiography images (resolution 512^2 pixels, 10 bits/pixel, see Fig. 2 for examples) during automatic rotation of the C-arm over 180 degrees lasting eight seconds. A modified filtered back-projection algorithm was then applied to generate 3DRA images at resolutions of 128^3 voxels of size $0.6^3\mathrm{mm}^3$ and 256^3 voxels of size $0.3^3\mathrm{mm}^3$, 16 bits/voxel.

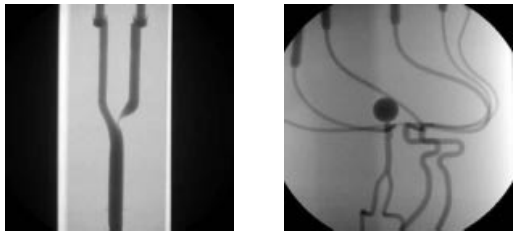

Fig. 2. Sample X-ray projection images taken from the rotational angiography runs of the CAVP (**left**) and the IAVP (**right**). The images give an impression of the morphology and complexity of the modeled vasculature.

Method of Evaluation. We first investigated the capabilities of the filtering techniques to reduce background noise while retaining vessel contrast as much as possible. To this end we measured the contrast-to-noise ratio (CNR) in each of the vessels of interest: $\mathrm{CNR} = (\langle I \rangle_{\mathcal{V}} - \langle I \rangle_{\mathcal{B}})^2 / \sigma^2_{\mathcal{B}}$, where I and σ^2 denote image intensity and variance, respectively, and $\mathcal{V}$ and $\mathcal{B}$ vessel and background regions. For $\mathcal{B}$, a fixed background region was selected in each of the images. The CNR was measured as a function of "evolution time", t. This variable is explicitly present in RPM and EED, and together with the temporal step-size Δt determines the number of iterations of the discretized differential equation to be carried out. For GF we have the relation $t = \sigma^2/2$. For UF we used the same relation, with σ the standard deviation of u_m, so that $t = m^2/24$, where m is a discrete variable for which we took values of $1, 3, 5, 7, 9$, and 11. To allow a direct comparison of the results of UF and GF, RPM, and EED, the measurements for the latter schemes were carried out at corresponding evolution times $t = 0.0$ (original), 0.375, 1.042, 2.042, 3.375, and 5.042. In all experiments,

the additional parameters of RPM and EED were fixed to $\sigma_n = 0.5$ and $\zeta = 0.05$, which seemed to be appropriate values according to initial experiments.

Next, the effects of the techniques on quantification of the vascular anomalies were investigated. Therefore, the diameters d_{S}, d_{ICA}, d_{CCA}, d_{N}, and d_{D} were measured as a function of both t and the threshold parameter θ. For t we used the same values as in the CNR measurements. The parameter θ is used in practice to separate relevant (vascular) from non-relevant (noise and other) structures in the visualizations, on the base of which quantification takes place. In order to use acquisition independent values for θ, the images were "normalized" so as to make the average background intensity 0.0 and the average intensity within the vessels 1.0. Together with the ground-truth values, the results allowed for an assessment of both accuracy and robustness to threshold selection of quantitative measurements and their dependency on the filter strength.

Finally, we looked at the qualitative (visual) effects of the different noise reduction techniques. These concerned the apparent (not measured) dimensions of the vascular anomalies in 3D visualizations of the filtered 3DRA datasets and their dependency on the user-controlled threshold parameter, as well as the apparent smoothness of the vascular structures in these visualizations. To this end, both exo- and endovascular surface renderings were generated by using a standard Phong shading technique.

Results. Because of space limitations we have to confine ourselves here to showing only some of the results and to summarize the overall findings. Examples of CNR measurement results carried out in high-resolution 3DRAs of the CAVP and IAVP are given in Fig. 3. The results showed that the four schemes UF, GF, RPM, and EED reduce noise equally well in vessel segments with a relatively large luminal diameter (typically larger than 10 voxels). For segments with smaller diameters, the nonlinear filtering techniques (RPM and EED) outperformed the linear techniques (UF and GF) for larger evolution times.

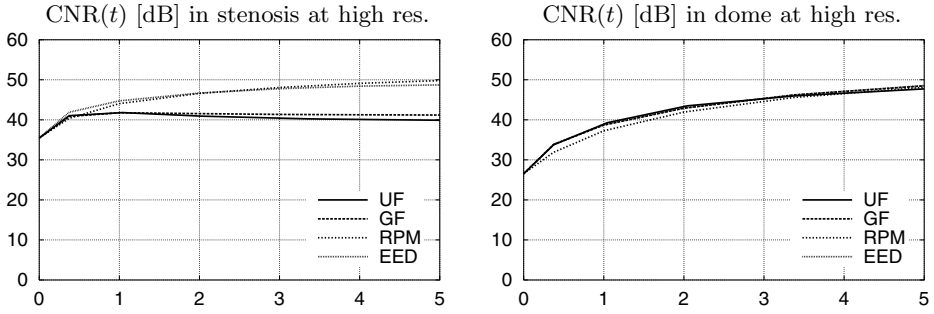

Fig. 3. Contrast-to-noise ratio (CNR) as a function of evolution time (t) for the four techniques (UF, GF, RPM, EED), measured in the stenosis (**left**) and dome (**right**) in the high-resolution 3DRA reconstruction of the CAVP and IAVP, respectively.

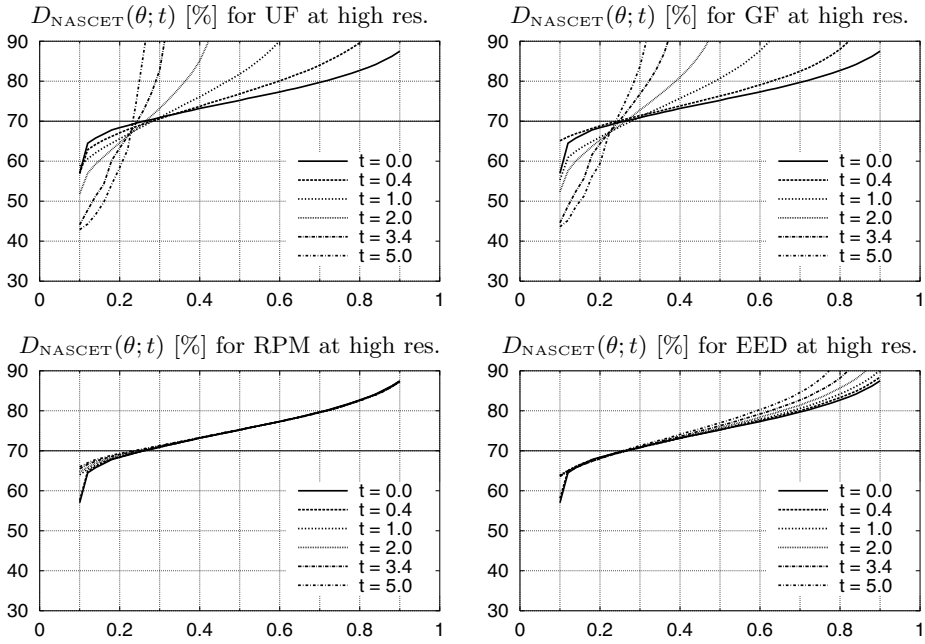

Fig. 4. Degree of stenosis (D_{NASCET}) as a function of the user-controlled threshold (θ) and evolution time (t) for the four techniques (UF, GF, RPM, EED), as measured in the high-resolution reconstruction of the CAVP. The true value is $D_{\mathrm{NASCET}} = 70\%$.

Whereas the CNR measurements concerned the behavior of the techniques in the background and the interior of vessels, the diameter measurements revealed their performance at the transitions from background to vessel. Examples of the results of these experiments are given in Fig. 4. These results showed that, as expected, the linear techniques (UF, GF) dramatically increase the dependency of the measurements on the user-controlled threshold parameter (θ) as the filtering was made stronger (larger t). The RPM scheme, on the other hand, had a negligible influence on this dependency, irrespective of evolution time. The effects of EED on the user-dependency were negligible only in the high-resolution 3DRAs, where all diameters were larger than about five voxels.

Finally, examples of exo- and endovascular surface renderings generated from the high-resolution 3DRA images of the CAVP and IAVP after application of the different techniques are shown in Figs. 5 and 6. The renderings show close-ups of the vascular anomalies and give a visual impression of the effects of the techniques on the smoothness of the vessel walls and the changes in the apparent dimensions of the anomalies when varying the user-controlled threshold. The renderings support the findings of the quantification experiments: the linear techniques increased the user-dependency of the vascular dimensions, while the negative effects of RPM and EED were marginal. The smoothness of the vessel

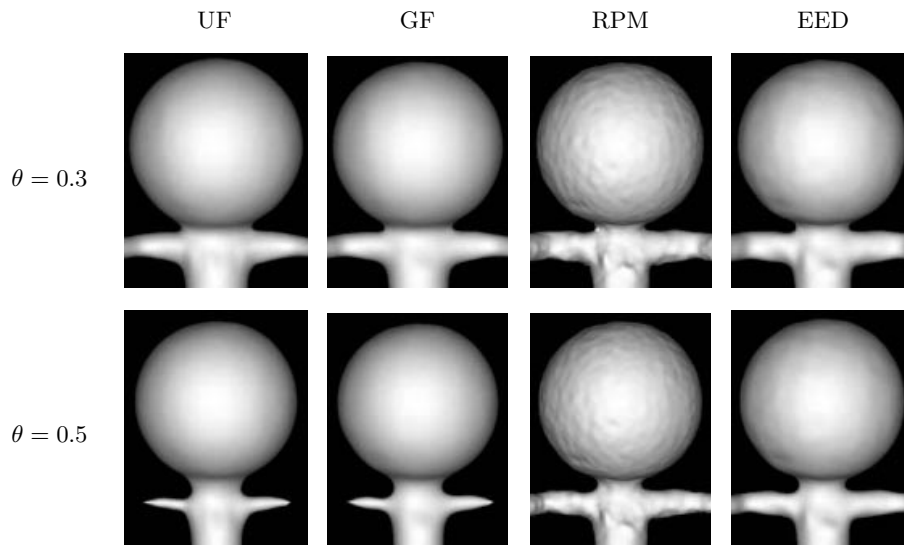

Fig. 5. Exovascular surface renderings of the IAVP illustrating the effects of the different techniques (UF, GF, RPM, EED) on the smoothness of the vessel walls and the apparent size of especially the neck of the aneurysm when varying the user-controlled threshold parameter (θ). The renderings show a close-up of the neck and the dome of the aneurysm, the BA and both PCAs, at $t = 2.042$.

walls, however, was considerably improved by EED, while most of the noise in these edge regions was retained by RPM.

5 Discussion and Conclusions

Overall, the results of our *in vitro* experiments suggest that for vessels with sufficiently large luminal diameter, EED is most suitable: the increase in the user-dependency of quantifications and visualizations is considerably less than with UF or GF, and it is better at reducing noise at the vessel walls than RPM. The sub-optimal performance of EED in vessel segments with very small luminal diameters is most probably due to the fact that the amount of blurring in the plane orthogonal to a local gradient is equal in all directions. We suspect that in order for EED to work adequately also in these cases, it is necessary to make a distinction between the directions corresponding to minimal and maximal curvature, which requires the use of second-order information (Hessian). Early experiments with curvature-based anisotropic diffusion schemes [12] have shown promising results, but more elaborate evaluations are required to determine the clinical implications. Other disadvantages of EED are its memory requirements and its relatively high computational cost. If these are decisive factors, RPM may be a reasonable alternative, for which more efficient algorithms exist [7].

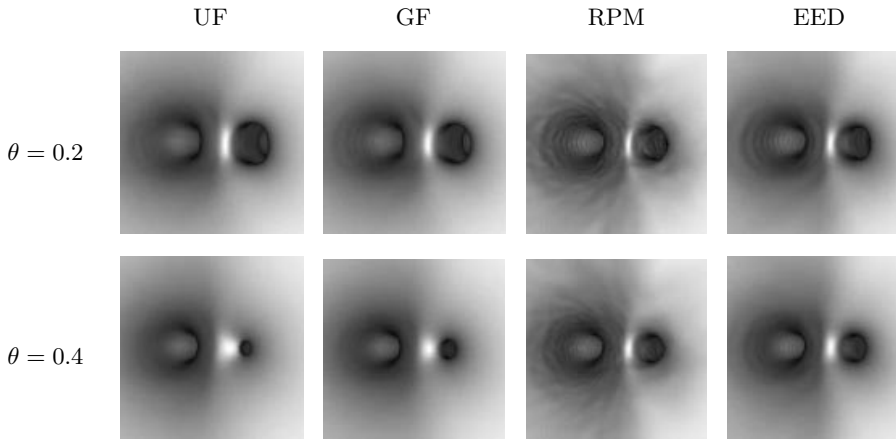

Fig. 6. Endovascular surface renderings of the CAVP illustrating the effects of the different techniques (UF, GF, RPM, EED) on the smoothness of the vessel walls and the apparent degree of stenosis when varying the user-controlled threshold parameter (θ). The renderings show the ECA (left passage) and the stenosis in the ICA (right passage), viewed from within the CCA, at $t = 2.042$.

References

1. R. Fahrig *et al.*, "Use of a C-arm system to generate true three-dimensional computed rotational angiograms: Preliminary *in vitro* and *in vivo* results", *Am. J. Neuroradiol.*, vol. 18, 1997, pp. 1507–1514.
2. B. A. Schueler *et al.*, "Three-dimensional vascular reconstruction with a clinical X-ray angiography system", *Acad. Radiol.*, vol. 4, 1997, pp. 693–699.
3. J. Moret *et al.*, "3D rotational angiography: Clinical value in endovascular treatment", *Medicamundi*, vol. 42, 1998, pp. 8–14.
4. R. Anxionnat *et al.*, "3D angiography: Clinical interest. First applications in interventional neuroradiology", *J. Neuroradiol.*, vol. 25, 1998, pp. 251–262.
5. Y. Trousset *et al.*, "A fully automated system for three-dimensional X-ray angiography", in *Computer Assisted Radiology and Surgery (CARS'99)*, Elsevier Science, Amsterdam, 1999, pp. 39–43.
6. F. Catté *et al.*, "Image selective smoothing and edge detection by nonlinear diffusion", *SIAM J. Num. Anal.*, vol. 29, 1992, pp. 182–193.
7. J. Weickert, *Anisotropic Diffusion in Image Processing*, B. G. Teubner, Stuttgart, Germany, 1998.
8. P. M. Rothwell *et al.*, "Equivalence of measurements of carotid stenosis. a comparison of three methods on 1001 angiograms", *Stroke*, vol. 25, 1994, pp. 2435–2439.
9. N. Yasui *et al.*, "Subarachnoid hemorrhage caused by previously diagnosed, previously unruptured intracranial aneurysms: A retrospective analysis of 25 cases", *Neurosurgery*, vol. 39, 1996, pp. 1096–1100.
10. A. Fernandez Zubillaga *et al.*, "Endovascular occlusion of intracranial aneurysms with electrically detachable coils: Correlation of aneurysm neck size and treatment results", *Am. J. Neuroradiol.*, vol. 15, 1994, pp. 815–820.

11. L. Parlea *et al.*, "An analysis of the geometry of saccular intracranial aneurysms", *Am. J. Neuroradiol.*, vol. 20, 1999, pp. 1079–1089.
12. K. Krissian *et al.*, "Directional anisotropic diffusion applied to segmentation of vessels in 3D images", in *Scale-Space Theory in Computer Vision*, vol. 1252 of *Lecture Notes in Computer Science*, Springer-Verlag, Berlin, 1997, pp. 345–348.